

Article

# First-Principles Point Defect Models for $Zr_7Ni_{10}$ and $Zr_2Ni_7$ Phases

Diana F. Wong<sup>1,2</sup>, Kwo-Hsiung Young<sup>1,2,\*</sup>, Taihei Ouchi<sup>2</sup> and K. Y. Simon Ng<sup>1</sup>

<sup>1</sup> Department of Chemical Engineering and Materials Science, Wayne State University, Detroit, MI 48202, USA; diana.f.wong@basf.com (D.F.W.); sng@wayne.edu (K.Y.S.N.)

<sup>2</sup> BASF/Battery Materials-Ovonic, 2983 Waterview Drive, Rochester Hills, MI 48309, USA; taihei.ouchi@basf.com

\* Correspondence: kwo.young@basf.com; Tel.: +1-248-293-7000

Academic Editor: Andreas Jossen

Received: 24 April 2016; Accepted: 28 June 2016; Published: 30 June 2016

**Abstract:** Synergetic effects in multi-phased  $AB_2$  Laves-phase-based metal hydride (MH) alloys enable the access of high hydrogen storage secondary phases, despite the lower absorption/desorption kinetics found in nickel/metal hydride (Ni/MH) batteries. Alloy design strategies to further tune the electrochemical properties of these secondary phases include the use of additives and processing techniques to manipulate the chemical nature and the microstructure of these materials. It is also of particular interest to observe the engineering of constitutional point defects and how they may affect electrochemical properties and performance. The  $Zr_7Ni_{10}$  phase appears particularly prone to point defects, and we use density functional theory (DFT) calculations coupled with a statistical mechanics model to study the theoretical point defects. The  $Zr_2Ni_7$  phase appears less prone to point defects, and we use the  $Zr_2Ni_7$  point defect model, as well as experimental lattice parameters, with  $Zr_7Ni_{10}$  phases from X-ray diffraction (XRD) as points of comparison. The point defect models indicate that anti-site defects tend to form in the  $Zr_7Ni_{10}$  phase, and that these defects form more easily in the  $Zr_7Ni_{10}$  phase than the  $Zr_2Ni_7$  phase, as expected.

**Keywords:** nickel/metal hydride (Ni/MH) battery; Zr-Ni intermetallics; point defects; density functional theory (DFT); statistical mechanics; modeling

## 1. Introduction

Nickel/metal hydride (Ni/MH) batteries utilizing multi-phased  $AB_2$  Laves-phase-based metal hydride (MH) alloy active materials leverage the synergetic effects between secondary phases and the main Laves phases to allow access to the high hydrogen storage of the secondary phases, such as  $Zr_7Ni_{10}$ , despite their lower absorption/desorption kinetics [1–5]. The  $Zr_2Ni_7$  phase, on the other hand, has excellent absorption/desorption kinetics, but poor hydrogen storage capacity [4,6]. Modifiers to the Zr-Ni alloys, including Ti in  $Ti_xZr_{7-x}Ni_{10}$ , have shown improvements in diffusion to help the kinetics [5], and V in  $ZrV_xNi_{3.5-x}$  has shown improvements in capacity [6]. In addition to modifiers, constitutional defect structures in the alloys may also affect mechanical and electrochemical properties. Defects, including vacancies, can act to trap hydrogen and inhibit the transport of hydrogen through the alloy [7]. In addition, other defects, such as anti-sites, can promote lower atomic packing ratios, which can improve the cycling capability due to a higher propensity to deform rather than to crack [8,9]. The ability to tune the ratio between hydride formers, such as Zr, and hydride modifiers, such as Ni, as well as to add other modifiers while maintaining the structure of the alloys is an important feature for designing battery materials targeting a specific application, and can strongly affect battery performance properties [10–13]. We have constructed point defect models for the  $Zr_7Ni_{10}$  and  $Zr_2Ni_7$  phases from first-principle calculations to lay the groundwork for examining how structure and defects can affect

properties that can be linked to Ni/MH battery performance, adding another dimension to consider in the design of negative active materials. Some comparison to experimental lattice parameters show a consistency with predicted defected structures and  $c/b$  lattice ratio trends.

## 2. Computational Details

Point defect models for intermetallics have been constructed and studied in the literature for binary compounds, such as ZrNi [14], FeAl [15,16], NiAl [17], and NiAl<sub>3</sub> [18]. We apply similar techniques and assumptions to construct the point defect models for the Zr<sub>7</sub>Ni<sub>10</sub> and Zr<sub>2</sub>Ni<sub>7</sub> phases (each with Zr-rich, stoichiometric, and Ni-rich cases); statistical mechanics use defect formation energies and the formation of defect combinations while preserving the targeted phase composition to provide defect compositions that minimize the potential energy of the system, and density functional theory (DFT) calculations supply the defect formation energies needed in the statistical mechanics model. The details in constructing the point defect models are described in Appendix. The *fsolve* function from the SciPy library for Python was used to solve the equations generated for vacancies and anti-site defects for each sublattice, defined by the equivalent atom sites in Zr<sub>7</sub>Ni<sub>10</sub> and Zr<sub>2</sub>Ni<sub>7</sub> phases (e.g.,  $4a$  sites comprise a single sublattice). We neglected dumbbell and interstitial defects, due to the limited space available near each of the sites. LaNi<sub>5</sub> is known to form dumbbell interstitials due to the hexagon-shaped holes above and below La on the  $z = 0$  plane [19]. Ni–Ni distances across the hexagon vertices measure  $\sim 5.1$  Å across with Ni–Ni bond lengths of  $\sim 2.5$  Å. Holes or spaces near the Zr local environment in Zr<sub>7</sub>Ni<sub>10</sub> and Zr<sub>2</sub>Ni<sub>7</sub> phases are typically pentagon- or square-shaped, with vertices measuring 3.8–4.7 Å and Ni–Ni bond lengths measuring  $\sim 2.6$ –2.8 Å. Defect concentrations and effective formation energies were calculated at a reference temperature of 1000 °C, a temperature near the melting points for the Zr<sub>7</sub>Ni<sub>10</sub> and Zr<sub>2</sub>Ni<sub>7</sub> systems [20]. When precision limitations were encountered in Python (typically at low temperature, which results in extremely low defect concentrations), the logarithmic terms containing defect concentration variables were analyzed and dropped when low concentration assumptions were valid.

Electronic structure calculations were performed using the plane-wave-based DFT code implemented in Quantum ESPRESSO (Version 5.1.0, Quantum ESPRESSO Foundation, London, UK) [21] and ultra-soft pseudopotentials from the Garrity–Bennett–Rabe–Vanderbilt (GBRV) Pseudopotential Library (Piscataway, NJ, USA) [22]. The exchange–correlation potential applied the Perdew–Burke–Ernzerhof (PBE) version of the generalized gradient approximation [23]. The recommended plane-wave cutoff energy of 40 Ry and charge-density cutoff energy of 120 Ry allowed convergence within  $1 \times 10^{-5}$  Ry/atom of the energy. A Methfessel–Paxton smearing width of 0.02 Ry with a Monkhorst–Pack k-point grid that yields 100–200 k-points also met convergence criteria with reasonable speed [24,25]. Spin-polarization was not included in the calculations, as differences in energies and stresses were low (<0.5 kbar) when included in the base equilibrium structures.

Cell structural optimizations for a given composition and structure were conducted by a variable cell relaxation calculation that minimizes forces and stresses within the cell. Symmetry of the cell was conserved during the structural optimizations based on a starting input structure. Non-defected structures preserved the symmetry based on starting experimental values. Using the optimized non-defected structure as a base, we removed or substituted atoms to create starting input values for the defected structures. The cell is considered optimized when forces were below  $1 \times 10^{-3}$  Ry/Å, the minimum energy converged at below  $1 \times 10^{-5}$  Ry/atom, and stresses converged within 0.5 kbar.

The Zr<sub>7</sub>Ni<sub>10</sub> phase has an orthorhombic structure and can sometimes occur as a metastable tetragonal phase [5,26,27]. It was originally reported to have space group symmetry *Aba2* [28,29] and has since been revised to have space group symmetry *Cmca* [30]. Its crystal structure is shown in Figure 1a, rendered using VESTA Graphical Software (Version 3.2.1, Momma and Izumi, Tsukuba, Japan) [31]. It contains 68 atoms per unit cell ( $Z = 4$  formula units) with experimental parameters  $a = 12.381$  Å,  $b = 9.185$  Å, and  $c = 9.221$  Å [30]. The unit cell contains four equivalent Zr atoms in the  $4a$ ,  $8d$ ,  $8e$ , and  $8f_1$  positions and three equivalent Ni atoms in the  $8f_2$ ,  $16g_1$ , and  $16g_2$  positions. A supercell

was not constructed due to the inherent large size of the cell. The structure with the space group *Aba2* was evaluated for the calculation and allowed to relax, yielding the energy of the non-defected structure. Point defects involving all equivalent sites of the optimized non-defected structure were also evaluated, obtaining the energy of each defected structure after relaxation.

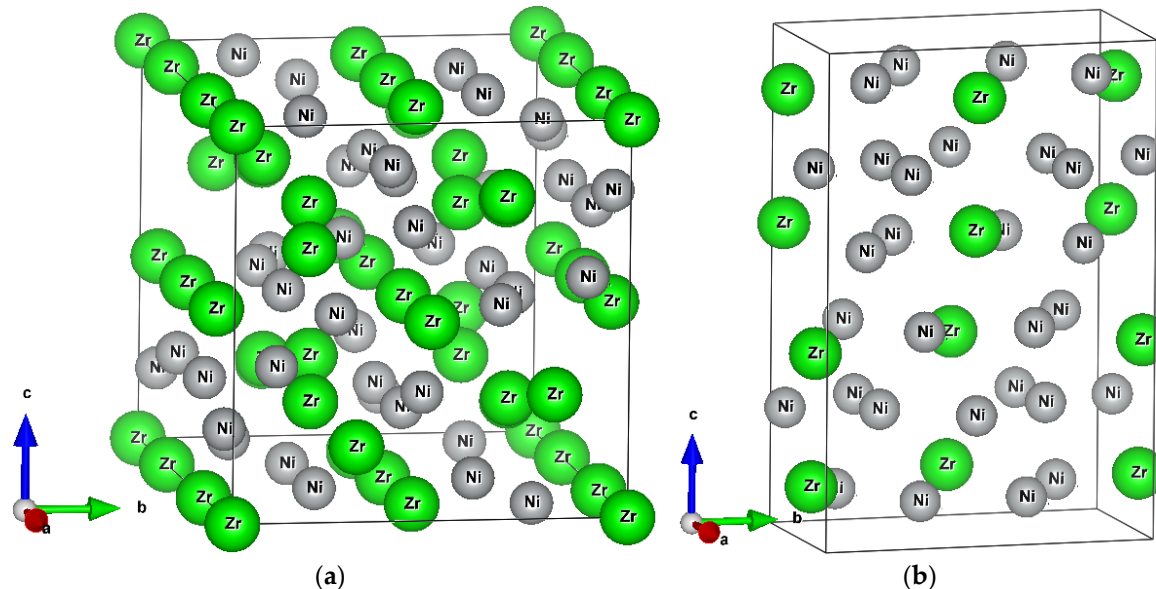


Figure 1. Unit-cell crystal structures for (a)  $Zr_7Ni_{10}$  and (b)  $Zr_2Ni_7$ .

The  $Zr_2Ni_7$  phase is monoclinic, and its crystal structure is shown in Figure 1b. It contains 36 atoms per unit cell ( $Z = 4$ ) with experimental parameters  $a = 4.698 \text{ \AA}$ ,  $b = 8.235 \text{ \AA}$ ,  $c = 12.193 \text{ \AA}$  and  $\beta = 95.83^\circ$  [32]. It contains two equivalent Zr atoms in the  $4i_1$  and  $4i_2$  positions and four equivalent Ni atoms in the  $4i_3$ ,  $8j_1$ ,  $8j_2$ , and  $8j_3$  positions. A  $2 \times 1 \times 1$  supercell containing 72 atoms was constructed to reduce interactions for the defects in adjacent cells. Point defects involving all equivalent sites were evaluated to obtain the energy of each defected structure after relaxation. The structures for  $ZrNi_5$  (cubic  $AuBe_5$  structure [33]),  $Zr_8Ni_{21}$  (triclinic  $Hf_8Ni_{21}$  structure [34]), and  $ZrNi$  (orthorhombic  $CrB$  structure [35]) were also optimized to calculate the energies that define the tie lines for the formation energy diagrams.

The point defect model is developed for stoichiometric and near stoichiometric compositions in which assumptions for low defect concentrations are valid and interactions between defects are considered negligible. Defect concentrations beyond  $\sim 1\%$  concentration would require a new model that considers defect interactions and the dependence of defect formation energy parameters on defect concentration.

### 3. Experimental Setup

Lattice parameters shrink with vacancy-predominant defects, and grow with certain anti-site defects (e.g.,  $Zr \rightarrow Ni$  anti-site defects). Experimental lattice parameters offer some evidence of the consistency of the  $Zr_7Ni_{10}$  point defect model. An arc melting process under continuous argon flow with a non-consumable tungsten electrode and water-cooled copper tray was used to prepare Zr-rich and Ni-rich  $Zr_7Ni_{10}$  ingot samples. Before each arc melt, a piece of sacrificial titanium was repeatedly melted and cooled for several cycles to reduce the residual oxygen concentration in the system. Similarly, each 5 g ingot was turned over, melted, and cooled several times to ensure uniformity in the chemical composition. A Rigaku Miniflex X-ray diffractometer (XRD, Rigaku, Tokyo, Japan) was used to study the phase component. JEOL-JSM32C and JEOL-JSM6400 scanning electron microscopes

(SEM, JEOL, Tokyo, Japan) with energy dispersive spectroscopy (EDS) were applied to investigating the phase distribution and composition.

## 4. Results and Discussion

### 4.1. Theoretical Point Defects in $Zr_7Ni_{10}$

DFT calculation of the  $Zr_7Ni_{10}$  phase in the space group  $Aba2$  results in a relaxed structure with a space group  $Cmca$  symmetry. The calculated lattice parameters are shown in Table 1, with comparative experimental lattice parameters. The lattice parameters show reasonable agreement with the experiment results, although the calculated structure appears to converge to a near tetragonal unit cell. This near tetragonal structure differs from the tetragonal meta-stable phase observed experimentally after hydrogenation–dehydrogenation of  $Zr_7Ni_{10}$  alloys; the dehydrogenated  $Zr_7Ni_{10}$  alloy has a smaller lattice parameter ( $a = b = 6.496 \text{ \AA}$ ) with different symmetry [5,26,27]. Constitutional point defects may play a role in the different structures that were observed and calculated for the  $Zr_7Ni_{10}$  phase, for example, by introducing distortion to the lattice that favors the orthorhombic unit cell. Defects and distortion to the crystal lattice may promote diffusion kinetics for improved rate performance and access to hydrogen storage capacity if energy barriers between hydrogen sites are lowered with the defects/distortion. We examine the relative ease with which defects can form by first calculating the DFT defect formation energies for the  $Zr_7Ni_{10}$  phase.

**Table 1.**  $Zr_7Ni_{10}$  unit-cell lattice parameters.

Parameter	This Work	References [28,29]	Reference [30]
Space group	<i>Cmca</i>	<i>Aba2</i>	<i>Cmca</i>
<i>a</i> (Å)	12.419	12.386	12.381
<i>b</i> (Å)	9.179	9.156	9.185
<i>c</i> (Å)	9.180	9.211	9.221
Unit-cell volume (Å <sup>3</sup> )	1046.5	1044.6	1048.6

#### 4.1.1. Density Functional Theory Defect Formation Energies

Ground state DFT formation energies (at  $T = 0 \text{ K}$ ) for  $Zr_7Ni_{10}$  phase and the theoretical Ni  $\rightarrow$  Zr anti-site, Zr vacancy, Ni vacancy, and Zr  $\rightarrow$  Ni anti-site defects are plotted in Figure 2 with the tie lines to the neighboring compounds  $Zr_8Ni_{21}$  and  $ZrNi$ . The formation energies were calculated using following the equation:

$$\Delta H_f = \frac{E(Zr_nNi_m) - \frac{n}{2}E(Zr_2) - \frac{m}{4}E(Ni_4)}{n + m} \quad (1)$$

where  $E(Zr_nNi_m)$  is the energy of the Zr-Ni compound in the structure of interest,  $E(Zr_2)$  is the energy of Zr in hexagonal close-packed structure, and  $E(Ni_4)$  is the energy of Ni in a face-centered-cubic structure. Tie lines connect the ground state DFT formation energies of neighboring equilibrium structures (e.g.,  $Zr_7Ni_{10}$  and  $Zr_8Ni_{21}$  phases), and represent the ground state energies of phase mixtures based on the overall Zr content (as opposed to a single phase with the same Zr content containing vacancy/anti-site defects). All of the defect energies at 0 K lie above the stoichiometric compound, as well as above the tie lines, indicating energy is required for the defects to form, and that the defects are in competition with formation of phases or mixtures of phases. There can be a large difference in formation energies between the investigated sublattice sites, and each type of defect appears to prefer different sites. Out of the Zr sublattices, the Ni  $\rightarrow$  Zr anti-site defect appears to preferentially form on the  $8e$  sublattice, while the Zr vacancy defect appears to prefer the  $4a$  sublattice. For the Ni sublattices, the Ni vacancy defect appears to preferentially form on one of the  $16g$  sublattices, while the Zr  $\rightarrow$  Ni anti-site defect appears to preferentially form on the  $8f_2$  sublattice. Note that defect formation energies on the  $16g_1$  and  $16g_2$  sublattices are similar and appear indistinguishable in Figure 2.

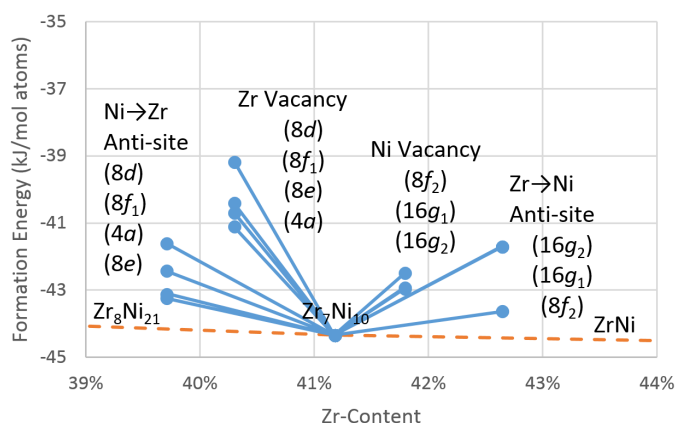


**Figure 2.** Density functional theory (DFT) formation energies for  $Zr_7Ni_{10}$  and its point defects with tie lines.

The model considers the effects of the heat of mixing, entropy, vibrational energy, and defect interaction on the free energy of each of the possible phases to be negligible, and a more comprehensive study of the point defect models could consider the effect of defect interactions. However, the DFT formation energies indicate that, out of the defects considered, the  $8e$  Ni  $\rightarrow$  Zr anti-site and the  $8f_2$  Zr  $\rightarrow$  Ni anti-site defects are the most stable of the point defects for the  $Zr_7Ni_{10}$  phase. However, since the  $Zr_7Ni_{10}$  phase is an ordered, binary compound, a mixture of all point defects is necessarily generated in order to maintain bulk homogeneity and required stoichiometry, and this is addressed by the statistical mechanics model (see Appendix).

#### 4.1.2. Theoretical Effective Defect Formation Model

The theoretical defect concentrations for  $Zr_7Ni_{10}$  phase at  $1000\text{ }^\circ\text{C}$  calculated from the statistical mechanics model using defect energy parameters derived from DFT calculations are plotted as functions of Zr-content for stoichiometric and theoretical off-stoichiometric compositions in Figure 3. Concentrations of defects for each of the different site sublattices were generated and combined to give a total concentration for a defect on the atomic sublattice. The A atoms represent Zr and the B atoms represent Ni in the binary statistical mechanics model, where  $c_v^{Zr}$  is the concentration of vacancies of the Zr sublattices,  $c_v^{Ni}$  is the concentration of vacancies of the Ni sublattices,  $c_{Ni}^{Zr}$  is the concentration of total Ni  $\rightarrow$  Zr anti-site defects, and  $c_{Zr}^{Ni}$  is the concentration of total Zr  $\rightarrow$  Ni anti-site defects.

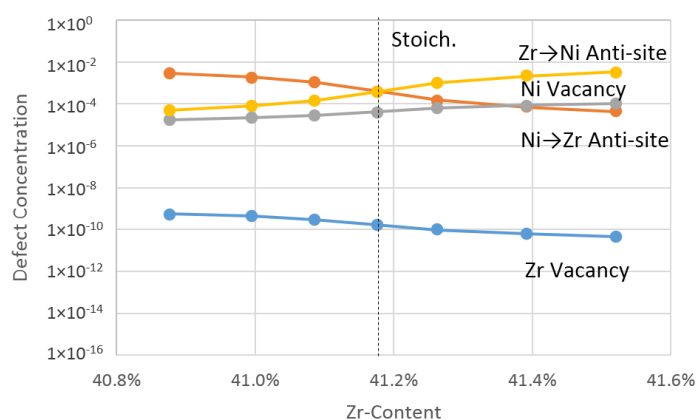


**Figure 3.** Theoretical defect concentrations for  $Zr_7Ni_{10}$  at  $1000\text{ }^\circ\text{C}$ .

The stoichiometric  $Zr_7Ni_{10}$  phase at  $1000\text{ }^\circ\text{C}$  is dominated by Ni  $\rightarrow$  Zr and Zr  $\rightarrow$  Ni anti-site defects in an approximately 1:1 ratio. Zr-rich compositions promote more defects of the Ni sublattices,

particularly Zr → Ni anti-site defects. Ni → Zr anti-site defects dominate the analysis for Ni-rich compositions, and while the concentration of Zr vacancies increases, it does not approach the concentrations of the other defects. Each of the defects in the sublattices generated an effective formation energy, and the weighted average by concentration of sublattice sites was used to calculate the theoretical effective formation energies of the atomic point defects. The theoretical effective formation energies for the respective point defects at 1000 °C are tabulated in Table 2 and show the relative ease at which the defects can form. The effective formation energies for the defects are consistent with the defect concentration trends observed in Figure 3, with Zr → Ni anti-site defects showing the lowest effective formation energy at stoichiometry and in the Zr-rich state.

**Table 2.** Theoretical effective formation energies for point defects in Zr<sub>7</sub>Ni<sub>10</sub> at 1000 °C.

Defects	Ni-Rich	Stoichiometric	Zr-Rich
$\Delta H_v^{\text{Zr}}$ (eV)	2.12	2.22	2.33
$\Delta H_v^{\text{Ni}}$ (eV)	1.10	1.03	0.95
$\Delta H_{\text{Ni}}^{\text{Zr}}$ (eV)	0.49	0.66	0.86
$\Delta H_{\text{Zr}}^{\text{Ni}}$ (eV)	0.80	0.63	0.44

The non-defected and defected unit-cell lattice parameters based on the structure that yielded the lowest DFT formation energy are tabulated in Table 3. Comparison of these calculated parameters to experimental lattice parameters, as measured by XRD, may offer some insight into the point defect structures that may occur in the Zr<sub>7</sub>Ni<sub>10</sub> phase.

**Table 3.** Unit-cell lattice parameters for non-defected and defected Zr<sub>7</sub>Ni<sub>10</sub>.

Parameters	Perfect Crystal	Zr Vacancy (4a)	Ni → Zr Anti-Site (8e)	Ni Vacancy (16g <sub>2</sub> )	Zr→Ni Anti-Site (8f <sub>2</sub> )
<i>a</i> (Å)	12.418	12.334	12.365	12.379	12.437
<i>b</i> (Å)	9.179	9.152	9.135	9.172	9.224
<i>c</i> (Å)	9.180	9.139	9.152	9.162	9.230
Unit-cell volume (Å <sup>3</sup> )	1046.4	1031.6	1033.7	1040.3	1058.8

We have noted that the calculated crystal structure for the stoichiometric Zr<sub>7</sub>Ni<sub>10</sub> phase based on parameters given in literature appears to converge towards a tetragonal unit cell. Experimental lattice parameters, however, show *c/b* lattice parameter ratios of 1.004–1.006 (~0.5% difference from the calculated value). Calculated anti-site defected lattice parameters also show *c/b* ratios >1, while vacancy defected lattice parameters show ratios <1. The point defect model for the Zr<sub>7</sub>Ni<sub>10</sub> phase presented here predicts higher concentrations of anti-site defects for stoichiometric and off-stoichiometric compositions. Curiously, the anti-site defected unit-cell aspect ratio trends appear more consistent to the experimental literature results than for the perfect crystal case (0.2% difference vs. 0.5% difference, respectively). This is despite experimental conditions that include an annealing treatment at a high temperature for a long period of time (one month) to obtain equilibrium phases [30]. We also note that the equilibrium phase diagram for the Ni-Zr system has been revised to correct the solubility window for the Zr<sub>7</sub>Ni<sub>10</sub> phase, originally reporting a Zr-content range of 41.1 at% to 43.5 at%, to a maximum threshold of 41.5 at% [20,27,36]. The relative difficulty in removing defects (or conversely, the relative ease of forming defects) in the Zr<sub>7</sub>Ni<sub>10</sub> phase could have led to the construction of the larger solubility window, which supports the case for the presence of anti-site defects at stoichiometric compositions, but does not reconcile the observation that the defects do not appear to be the most thermodynamically favorable structures, based on the assumptions made in these calculations. Possible future work can re-examine the assumptions involved in calculating the free energies of the non-defected and defected Zr<sub>7</sub>Ni<sub>10</sub> phase, taking into account effects of temperature on vibrational and entropic contributions. Supercells with both Zr → Ni and Ni → Zr anti-site defects

for stoichiometric compositions can be examined for possible interactive configurations and optimized for comparison.

In considering the types of point defects for the  $Zr_7Ni_{10}$  phase that may promote better electrochemical performance in Ni/MH batteries, the  $Zr \rightarrow Ni$  anti-site defects that are prevalent in Zr-rich phases offer a slightly larger unit-cell volume for hydrogen storage, lowering the plateau pressure and stabilizing the hydride and hydrogen storage sites. Conversely, the  $Ni \rightarrow Zr$  anti-site defects that are prevalent in Ni-rich phases slightly reduce the unit-cell volume, destabilizing the hydride and hydrogen storage sites.  $Zr \rightarrow Ni$  anti-site defects may also further locally trap hydrogen, with Zr strongly binding to hydrogen (heats of hydride formation are  $-163 \text{ kJ} \cdot \text{mol}^{-1}$  for metallic Zr [37] and  $-50 \text{ kJ} \cdot \text{mol}^{-1}$  for  $Zr_7Ni_{10}$  [5]). However, the effects of these defects on hydrogen storage capacity and reversibility appear incremental compared to the direct effects of structure and the hydrogen binding energy related to the ratio of hydride formers (Zr) and modifiers (Ni) in the alloy composition, which would need to be considered for comparing properties across different phases, such as the  $Zr_7Ni_{10}$  and  $Zr_2Ni_7$  phases. For example, the effect of hydrogen binding with higher Zr content can be seen in the reversibility performance ( $Zr_7Ni_{10}$  phase has a Zr/Ni ratio of 0.70 with 77% reversible capacity and an initial capacity of 1.01 hydrogen to metal (H/M), while  $Zr_2Ni_7$  phase has a Zr/Ni ratio of 0.29 with 100% reversible capacity and an initial capacity of 0.29 H/M [4]; the point defect models predict defect concentrations of  $10^{-5}$ – $10^{-3}$  at stoichiometry for local site effects). Within a single phase, however, insights may be gleaned for future alloy design, particularly since synergetic effect studies show that  $Zr_7Ni_{10}$  is a good catalytic phase, and improving its thermodynamic properties can further improve the performance of multi-phase negative electrode active materials [1]. One such strategy is to try to maintain the  $Zr_7Ni_{10}$  crystal structure, while substituting elements that have less of an affinity for hydrogen (Ti has a heat of hydrogen formation of  $-124 \text{ kJ} \cdot \text{mol}^{-1}$  [37]) while balancing lattice shrinkage with combination of anti-site defects and other additives. The point defect models offer a first step towards laying the groundwork for understanding the role of constitutional defects as it relates to alloy design and optimization of electrochemical properties for Ni/MH batteries. Investigation of absorption–desorption or diffusion kinetics, through the calculation of the activation energy by methods such as nudged elastic band, can be of interest. Future work involving additives can also offer further tuning of the defect structures; addition of Ti has experimentally improved hydrogen reversibility, as well as the kinetics needed for high-rate discharge [5].

#### 4.2. Theoretical Point Defects in $Zr_2Ni_7$

The  $Zr_2Ni_7$  phase was studied to provide a comparison to the  $Zr_7Ni_{10}$  phase in terms of the types of defects formed and the ease of defect formation. The DFT structure optimization calculation for the  $Zr_2Ni_7$  phase is consistent with the monoclinic  $C2/m$  symmetry and structure reported in literature. The calculated lattice parameters are shown in Table 4 with experimental comparative lattice parameters. The lattice parameters show reasonable agreement with the experimental results. The DFT defect formation energies for the  $Zr_2Ni_7$  phase are calculated based on this optimized calculated structure.

**Table 4.**  $Zr_2Ni_7$  unit-cell lattice parameters.

Lattice Parameter	This Work	From Reference [32]
$a$ (Å)	4.677	4.698
$b$ (Å)	8.239	8.235
$c$ (Å)	12.176	12.193
$\beta$ (°)	95.20	95.83

##### 4.2.1. Density Functional Theory Formation Energies

Ground state DFT formation energies for the  $Zr_2Ni_7$  phase and its theoretical  $Ni \rightarrow Zr$  anti-site, Zr vacancy, Ni vacancy, and  $Zr \rightarrow Ni$  anti-site defects are plotted in Figure 4, with tie lines to

neighboring compounds  $ZrNi_5$  and  $Zr_8Ni_{21}$ . All defect energies at 0 K lie above that of the stoichiometric compounds, as well as the tie lines. However, the  $Ni \rightarrow Zr$  anti-site defect energy lies considerably higher than the stoichiometric compound and the  $ZrNi_5$ - $Zr_2Ni_7$  mixture tie line, indicating a possible shift in the dominating defects found in a Ni-rich compound. The  $Zr \rightarrow Ni$  anti-site defect energy is the lowest of the defects for the  $Zr_2Ni_7$  phase, followed by the Ni vacancy defect energy. There is a small difference in defect energy between the  $4i$  and  $8j$  sites for the Ni vacancy defect, but there is a larger difference between the sites of the  $Zr \rightarrow Ni$  anti-site defect. In general, point defects appear to form preferentially in the  $8j$  sublattices. Note that defect formation energies for several sets of sublattices are similar and appear indistinguishable in Figure 4 (i.e.,  $4i_1$  and  $4i_2$ ,  $4i_3$  and  $8j_3$ , and  $8j_1$  and  $8j_2$ ).

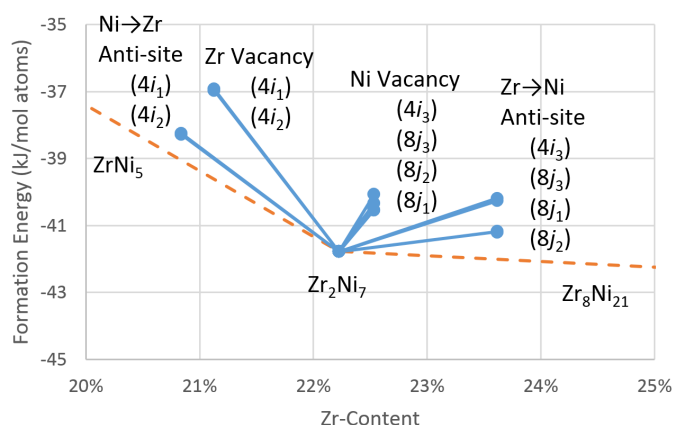


**Figure 4.** Formation energies for  $Zr_2Ni_7$  and its point defects with tie lines.

#### 4.2.2. Theoretical Effective Defect Formation Model

The theoretical defect concentrations for the  $Zr_2Ni_7$  phase at 1000 °C are plotted as functions of Zr-content in Figure 5. Stoichiometric  $Zr_2Ni_7$  phase at 1000 °C is dominated by Ni vacancy defects.  $Zr \rightarrow Ni$  anti-site defects overtake the formation of Ni vacancy defects in Zr-rich compositions, making  $Ni \rightarrow Zr$  anti-site defects the predominant defect for Ni-rich compositions. Zr vacancy defects also increase on the Ni-rich side, but again, the concentration is overall relatively low.

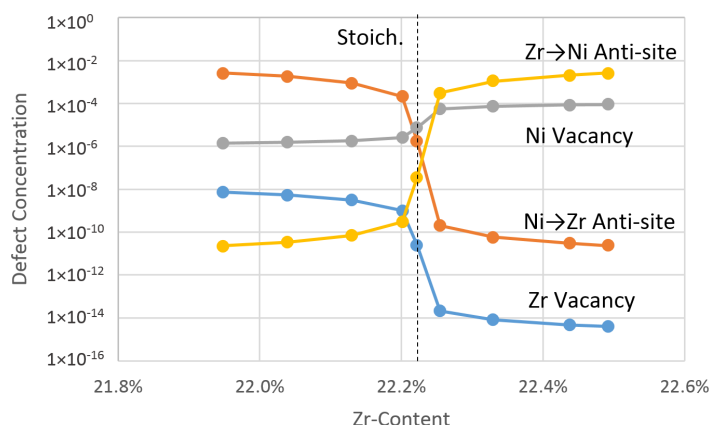


**Figure 5.** Theoretical defect concentrations for  $Zr_2Ni_7$  at 1000 °C.

The weighted theoretical effective formation energies for the respective point defects at 1000 °C are tabulated in Table 5 and define the relative ease for which a particular defect can form. The effective formation energies for the defects are consistent with the defect concentration trends observed in

Figure 5, with Ni vacancies showing the lowest effective formation energy at stoichiometric ratios. By comparing the point defect models between the  $Zr_7Ni_{10}$  and  $Zr_2Ni_7$  phases, the data suggests that it is easier to form defects in the  $Zr_7Ni_{10}$  phase than the  $Zr_2Ni_7$  phase, which is consistent with our hypothesis.

**Table 5.** Theoretical effective formation energies for point defects in  $Zr_2Ni_7$  at 1000 °C.

Defects	Ni-Rich	Stoichiometric	Zr-Rich
$\Delta H_v^{Zr}$ (eV)	1.89	2.52	3.47
$\Delta H_v^{Ni}$ (eV)	1.42	1.24	0.97
$\Delta H_{Ni}^{Zr}$ (eV)	0.48	1.29	2.52
$\Delta H_{Zr}^{Ni}$ (eV)	2.60	1.79	0.56

In considering the types of point defects within the  $Zr_2Ni_7$  phase that may promote better electrochemical performance in Ni/MH batteries, we again express caution for comparing different phases, but within the  $Zr_2Ni_7$  phase, Zr → Ni anti-site defects that are prevalent in Zr-rich phases offer a slightly larger unit-cell volume for hydrogen storage at the expense of possible hydrogen trapping, due to local Zr concentrations. Conversely, Ni → Zr anti-site defects that are prevalent in Ni-rich phases slightly reduce the unit-cell volume and, thereby, offer less space to accommodate hydrogen storage.

#### 4.3. Experimental Zr-Rich and Ni-Rich $Zr_7Ni_{10}$ Phase Analysis

The Zr-rich and Ni-rich  $Zr_7Ni_{10}$  alloy samples were used to compare their experimental lattice parameters to defected lattice parameters, as predicted by the model and calculated from DFT. No annealing treatment was applied to the samples to preserve meta-stable, off-stoichiometric phases. Representative SEM images of the Zr-rich sample are shown in Figure 6a,b, and their phase compositions, represented by differing contrasts in the images, are analyzed by EDS and listed in Table 6. The stoichiometric  $Zr_7Ni_{10}$  phase has a B/A ratio of 1.43 (where B = Ni, Al, and Mn and A = Zr), and the SEM-EDS analysis shows that the sample is mainly composed of a Zr-rich phase and smaller distributions of a Ni-rich phase, with a small presence of the  $Zr_2Ni$  phase. There is a small amount of Mn contamination in this sample, which may affect the interpretation of the results. However, previous first-principle calculations investigating substitutions in  $LaNi_5$  and  $TiMn_2$  alloys suggest that Mn and Ni substitutions do not alter the alloys' hydrogen stability sites, which offers an indication that the small amount of observed contamination may also have little effect [38]. A representative SEM image of the Ni-rich sample is shown in Figure 6c, with the phase composition listed similarly in Table 6. The analysis shows that the second sample is composed mainly of Ni-rich phases with the minor presence of the  $Zr_2Ni$  phase. Contamination was not detected in this particular sample.

**Table 6.** Energy dispersive spectroscopy (EDS) phase compositions of select areas for Zr-rich and Ni-rich  $Zr_7Ni_{10}$  alloy samples depicted in Figure 6.

Sample	Area	Zr	Ni	Al	Mn	B/A	Phase
Zr-rich $Zr_7Ni_{10}$	1	42.6	57.3	0.0	0.1	1.35	$Zr_7Ni_{10}$
	2	35.6	64.4	0.0	0.1	1.81	$Zr_7Ni_{10}$
	3	38.4	59.4	0.0	2.2	1.60	$Zr_7Ni_{10}$
	4	66.0	33.9	0.0	0.1	0.52	$Zr_2Ni$
Ni-rich $Zr_7Ni_{10}$	1	40.4	59.6	0.0	0.0	1.48	$Zr_7Ni_{10}$
	2	39.9	60.1	0.0	0.0	1.51	$Zr_7Ni_{10}$
	3	40.3	59.7	0.0	0.0	1.48	$Zr_7Ni_{10}$
	4	40.2	59.8	0.0	0.0	1.49	$Zr_7Ni_{10}$
	5	68.0	32.0	0.0	0.0	0.47	$Zr_2Ni$
	6	59.9	40.1	0.0	0.0	0.67	$Zr_2Ni$

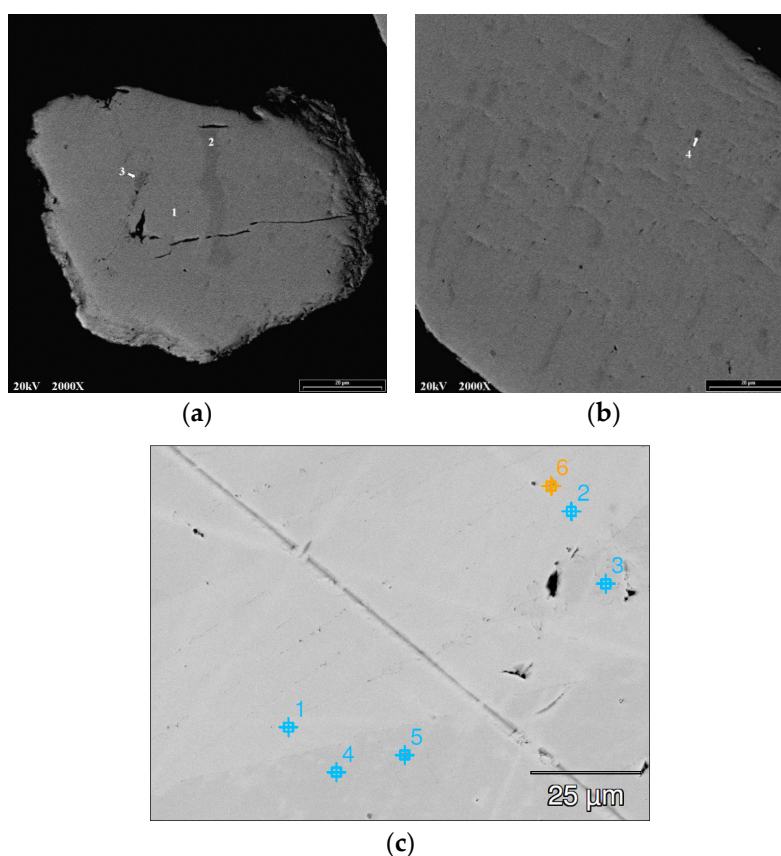


**Figure 6.** Scanning electron microscopy (SEM) images of a Zr-rich  $Zr_7Ni_{10}$  alloy sample showing representative phase distributions of (a) mainly Zr-rich phase and a smaller distribution of Ni-rich phases with (b) the presence of some amount of the  $Zr_2Ni$  phase; and (c) a Ni-rich  $Zr_7Ni_{10}$  alloy sample consisting of mainly Ni-rich phase and the presence of some amount of the  $Zr_2Ni$  phase. The bar on the right lower corner of the Zr-rich samples indicates a length of 20  $\mu m$ . Chemical compositions associated with the numbered areas are listed in Table 6.

Experimental lattice parameters for the Zr-rich and Ni-rich  $Zr_7Ni_{10}$  samples were obtained from XRD measurement, and are listed in Table 7. In comparison to the theoretical and experimental lattice parameters for the stoichiometric  $Zr_7Ni_{10}$  phase, both off-stoichiometric samples show unit cells that are smaller than expected. However, the Zr-rich sample shows a larger unit cell than the Ni-rich samples, which is consistent with expectations. The  $c/b$  ratios are also  $>1$ , which is consistent with the anti-site defected structures predicted by the point defect model.

**Table 7.** Experimental lattice parameters for Zr-rich and Ni-rich  $Zr_7Ni_{10}$  samples.

Parameter	Zr-Rich $Zr_7Ni_{10}$	Ni-Rich $Zr_7Ni_{10}$
$a$ (Å)	12.365	12.356
$b$ (Å)	9.172	9.162
$c$ (Å)	9.208	9.194
Unit-cell volume (Å <sup>3</sup> )	1044.2	1040.7

## 5. Conclusions

Defect models for the  $Zr_7Ni_{10}$  and  $Zr_2Ni_7$  intermetallic phases were calculated from first-principles using DFT and statistical mechanics. Zr-Ni based active negative electrode materials in Ni/MH batteries offer performance benefits such as improved capacity through synergetic phase

effects, and the understanding and engineering of point defects can contribute to further improvement in these materials through the framework that is laid by the defect models. DFT calculations confirmed that the  $Zr_7Ni_{10}$  phase structure has space group  $Cmca$  symmetry in the ground state. The point defect model indicates that at stoichiometry, the  $Zr_7Ni_{10}$  phase tends to form  $Zr \rightarrow Ni$  and  $Ni \rightarrow Zr$  anti-site defects in a 1:1 ratio, while  $Zr_2Ni_7$  tends to form Ni vacancy defects. Zr vacancies appear almost negligible in both  $Zr_7Ni_{10}$  and  $Zr_2Ni_7$  compounds.  $Zr \rightarrow Ni$  anti-site defects are the most prevalent defects in Zr-rich compositions in both compounds, and  $Ni \rightarrow Zr$  anti-site defects are the most prevalent defects in Ni-rich compositions. In general, it is easier to form defects in the  $Zr_7Ni_{10}$  phase than the  $Zr_2Ni_7$  phase. Comparison to experimental lattice parameters for the  $Zr_7Ni_{10}$  phase from XRD measurements show some discrepancy ( $\sim 0.5\%$  difference in  $c/b$  ratios) with regard to the orthorhombic versus tetragonal unit cells predicted by first principle calculations, which warrants further re-examination of the typical assumptions, as well as supercells that consider the distribution and interaction of defects in the calculations. Despite this discrepancy, the experimental lattice trends for off-stoichiometric phases ( $c/b$  ratios  $> 1$ ) appear to be consistent with the anti-site defects and the  $c/b$  ratios predicted by the model. The point defect models can be used to further investigate absorption–desorption or diffusion kinetics through nudged elastic band DFT calculations, offering further tuning of alloy design and the optimization of electrochemical properties for Ni/MH batteries.

**Acknowledgments:** The authors would like to thank the following individuals from BASF-Ovonic for their help: Jean Nei, David Pawlik, Alan Chan, Ryan J. Blankenship, and Su Cronogue.

**Author Contributions:** Kwo-Hsiung Young and Diana F. Wong conceived and designed the experiments; Diana F. Wong and Taihei Ouchi performed the experiments; Kwo-Hsiung Young, Diana F. Wong, Taihei Ouchi, and K. Y. Simon Ng analyzed the data; Diana F. Wong prepared the manuscript.

**Conflicts of Interest:** The authors declare no conflict of interest.

## Appendix

Defect models for  $Zr_7Ni_{10}$  and  $Zr_2Ni_7$  intermetallic phases are developed using statistical mechanics within the generalized grand canonical  $\mu PT$  formalism for an ordered, binary system  $A_nB_m$ , where Zr is an A-site atom and Ni is a B-site atom. The model is similar to the ones developed for NiAl [17] and NiAl<sub>3</sub> [18] systems, but is extended to account for a variable number of sublattices for each type of atom. These statistical mechanics-based models address the issue of non-homogeneity that can occur if we apply a monatomic crystal defect model wherein the formation energy of a vacancy defect is described by removing an atom and inserting it at a surface site; hypothetically by analogy in a binary system, A-site vacancies in an  $A_{0.5}B_{0.5}$  crystal would generate a surface of strictly A atoms, introducing non-homogeneity into the system [16,39]. To maintain homogeneity and composition of the bulk, such A-site vacancies are then necessarily accompanied by B-site vacancies,  $A \rightarrow B$  anti-site defects, or a mixture of the defects. The statistical mechanics model considers the different possible local defect configurations possible, minimizing the system potential to obtain equilibrium concentrations of each type of defect.

The system is described on a unit cell basis, so that  $n = 28$  and  $m = 40$  for  $Zr_7Ni_{10}$  phase and  $n = 8$  and  $m = 28$  for  $Zr_2Ni_7$  phase. The generalized grand canonical formalism prescribes the independent variable temperature  $T$ , pressure  $P$ , and chemical potential  $\mu_A$  and  $\mu_B$ . The generalized grand canonical potential  $J'$  is defined as:

$$J' = U + PV - TS - \mu_A N_A - \mu_B N_B \quad (A1)$$

where  $U$  is the internal energy of the system,  $V$  is the volume,  $S$  is the entropy,  $N_A$  is the number of A atoms in the system, and  $N_B$  is the number of B atoms in the system. The equilibrium concentrations of each type of point defect are found by minimizing the potential with respect to the concentration  $c_i^v$  or particle number  $N_i^v$  of each type of defect  $i$  (vacancy or anti-site) on the sublattice  $v$ . Each system contains  $M$  total possible lattice sites, which may be divided into sublattices  $\alpha$  for A-site atoms and  $\beta$  for B-site atoms. The sublattices can be further subdivided into  $\alpha_1, \alpha_2, \dots, \alpha_k$ , and  $\beta_1, \beta_2, \dots, \beta_l$ ,

for  $k$  equivalent A atoms and  $l$  equivalent B atoms. For example in the  $Zr_7Ni_{10}$  phase, we assign  $4a$ ,  $8d$ ,  $8e$ , and  $8f_1$  sites for the Zr atoms to sublattices  $\alpha_1$ ,  $\alpha_2$ ,  $\alpha_3$ , and  $\alpha_4$ , respectively, and  $8f_2$ ,  $16g_1$ , and  $16g_2$  sites for the Ni atoms to sublattices  $\beta_1$ ,  $\beta_2$ , and  $\beta_3$ , respectively.  $M$  is then also the sum of the lattice sites for each of the sublattices:

$$M = \sum_k M^{\alpha_k} + \sum_l M^{\beta_l} \quad (A2)$$

where  $M^{\alpha_k}$  is the total number of lattice sites for the  $\alpha_k$  sublattice and  $M^{\beta_l}$  is the total number of lattice sites for the  $\beta_l$  sublattice. The number of A and B atoms  $N_A$  and  $N_B$  in the system that can occupy the lattice sites is described by the accounting of the lattice sites and the number of defects:

$$N_A = \sum_k M^{\alpha_k} - \sum_k N_v^{\alpha_k} - \sum_k N_B^{\alpha_k} + \sum_l N_A^{\beta_l} \quad (A3)$$

$$N_B = \sum_l M^{\beta_l} - \sum_l N_v^{\beta_l} - \sum_l N_A^{\beta_l} + \sum_k N_B^{\alpha_k} \quad (A4)$$

where  $N_v^{\alpha_k}$  is the number of vacancy defects on the  $\alpha_k$  sublattice,  $N_B^{\alpha_k}$  is the number of B  $\rightarrow$  A antisite defects on the  $\alpha_k$  sublattice,  $N_v^{\beta_l}$  is the number of vacancy defects on the  $\beta_l$  sublattice, and  $N_A^{\beta_l}$  is the number of A  $\rightarrow$  B antisite defects on the  $\beta_l$  sublattice.

The internal energy  $U$  can be described as a sum of the ground state energy of the non-defected system and the defect formation energies:

$$U = M\varepsilon_0 + \sum_k N_v^{\alpha_k} \varepsilon_v^{\alpha_k} + N_B^{\alpha_k} \varepsilon_B^{\alpha_k} + \sum_l N_v^{\beta_l} \varepsilon_v^{\beta_l} + N_A^{\beta_l} \varepsilon_A^{\beta_l} \quad (A5)$$

The ground state energy per atom  $\varepsilon_0$  and the defect formation energy parameters  $\varepsilon_i^v$  are calculated from DFT using a supercell of  $N$  total lattice sites, such that

$$\varepsilon_0 = \frac{1}{N} E(N, 0) \quad (A6)$$

$$\varepsilon_v^{\alpha_k, \beta_l} = E(N - 1, 1^{\alpha_k, \beta_l}) - E(N, 0) \quad (A7)$$

$$\varepsilon_A^{\beta_l} = E(N, A^{\beta_l}) - E(N, 0) \quad (A8)$$

$$\varepsilon_B^{\alpha_k} = E(N, B^{\alpha_k}) - E(N, 0) \quad (A9)$$

where  $E(N, 0)$  is the ground state energy of the supercell of size  $N$  with zero defects,  $E(N - 1, 1^{\alpha_k, \beta_l})$  is the ground state energy of the supercell of size  $N - 1$  with one vacancy on the respective sublattice,  $E(N, A^{\beta_l})$  is the ground state energy of the supercell of size  $N$  with one A atom on the  $\beta_l$  sublattice, and  $E(N, B^{\alpha_k})$  is the ground state energy of the supercell of size  $N$  with one B atom on the  $\alpha_k$  sublattice. For low defect concentrations and cases near stoichiometry, the defects are assumed to be non-interacting so that  $\varepsilon_i^v$  does not change with concentration.

The volume of the system can also be written as a sum of its equilibrium volume in the non-defected state and the changes in the volume due to its defects:

$$V = Mv_0 + \sum_k N_v^{\alpha_k} v_v^{\alpha_k} + N_B^{\alpha_k} v_B^{\alpha_k} + \sum_l N_v^{\beta_l} v_v^{\beta_l} + N_A^{\beta_l} v_A^{\beta_l} \quad (A10)$$

where  $v_0$  is the unit-cell volume per atom and  $v_i^v$  is the defect volume formation parameter for defect  $i$  on sublattice  $\nu$ , defined similarly as in Equations (A6)–(A9).

The entropy  $S$  is the sum of the equilibrium entropy in the non-defected state, the defect formation entropies, and the configurational entropy:

$$S = Ms_0 + \sum_k N_v^{\alpha_k} s_v^{\alpha_k} + N_B^{\alpha_k} s_B^{\alpha_k} + \sum_l N_v^{\beta_l} s_v^{\beta_l} + N_A^{\beta_l} s_A^{\beta_l} + k_B \ln \left( \prod_k \frac{M^{\alpha_k}!}{N_v^{\alpha_k}! N_B^{\alpha_k}! (M^{\alpha_k} - N_v^{\alpha_k} - N_B^{\alpha_k})!} \cdot \prod_l \frac{M^{\beta_l}!}{N_v^{\beta_l}! N_A^{\beta_l}! (M^{\beta_l} - N_v^{\beta_l} - N_A^{\beta_l})!} \right) \quad (\text{A11})$$

where  $s_0$  is the entropy per atom in the non-defected structure and  $s_i^v$  is the defect entropy formation parameter for defect  $i$  on sublattice  $v$ , defined similarly as in Equations (A6)–(A9). Concentrations for each type of defect  $c_i^v$  can be derived by substituting Equations (A3)–(A5), (A10) and (A11) into Equation (A1) and minimizing the potential with respect to  $N_i^v$ , such that:

$$c_v^{\alpha_k} = \frac{N_v^{\alpha_k}}{M} = \frac{M^{\alpha_k}}{M} \frac{e^{s_v^{\alpha_k}/k_B} e^{-(\varepsilon_v^{\alpha_k} + \mu_A + P v_v^{\alpha_k})/k_B T}}{1 + e^{s_v^{\alpha_k}/k_B} e^{-(\varepsilon_v^{\alpha_k} + \mu_A + P v_v^{\alpha_k})/k_B T} + e^{s_B^{\alpha_k}/k_B} e^{-(\varepsilon_B^{\alpha_k} + \mu_A - \mu_B + P v_B^{\alpha_k})/k_B T}} \quad (\text{A12})$$

$$c_B^{\alpha_k} = \frac{N_B^{\alpha_k}}{M} = \frac{M^{\alpha_k}}{M} \frac{e^{s_B^{\alpha_k}/k_B} e^{-(\varepsilon_B^{\alpha_k} + \mu_A - \mu_B + P v_B^{\alpha_k})/k_B T}}{1 + e^{s_v^{\alpha_k}/k_B} e^{-(\varepsilon_v^{\alpha_k} + \mu_A + P v_v^{\alpha_k})/k_B T} + e^{s_B^{\alpha_k}/k_B} e^{-(\varepsilon_B^{\alpha_k} + \mu_A - \mu_B + P v_B^{\alpha_k})/k_B T}} \quad (\text{A13})$$

Similar expressions are derived for  $c_v^{\beta_l}$  and  $c_A^{\beta_l}$ .

The chemical potentials  $\mu_A$  and  $\mu_B$  are Lagrangian parameters that can be determined from the thermodynamic relation  $J' = 0$  for the generalized grand canonical potential [16]. From this relation, we combine Equations (A1), (A5) and (A10)–(A13) and their analogous expressions to obtain:

$$\begin{aligned} \varepsilon_0 + P v_0 - T s_0 &= \sum_k \frac{M^{\alpha_k}}{M} \mu_A + \sum_l \frac{M^{\beta_l}}{M} \mu_B \\ &- \sum_k \frac{M^{\alpha_k}}{M} k_B T \ln \left( 1 - \frac{M}{M^{\alpha_k}} c_v^{\alpha_k} - \frac{M}{M^{\alpha_k}} c_B^{\alpha_k} \right) \\ &- \sum_l \frac{M^{\beta_l}}{M} k_B T \ln \left( 1 - \frac{M}{M^{\beta_l}} c_v^{\beta_l} - \frac{M}{M^{\beta_l}} c_A^{\beta_l} \right) \end{aligned} \quad (\text{A14})$$

A final expression describing the composition of the compound preserves the composition of the compound of the system of interest:

$$\frac{N_A}{N_B} = \frac{\sum_k M^{\alpha_k} - \sum_k N_B^{\alpha_k} - \sum_k N_v^{\alpha_k} + \sum_l N_A^{\beta_l}}{\sum_l M^{\beta_l} - \sum_l N_A^{\beta_l} - \sum_l N_v^{\beta_l} + \sum_k N_B^{\alpha_k}} = \frac{x}{1-x} \quad (\text{A15})$$

where  $x$  is the atomic fraction of A atoms of the system  $A_x B_{1-x}$ .

The effective formation energy of the atomic defects is defined as:

$$\Delta H_i^v = -k_B \frac{\partial c_i^v}{\partial \left( \frac{1}{T} \right)} \quad (\text{A16})$$

which simplifies to

$$\Delta H_v^{\alpha_k} = \varepsilon_v^{\alpha_k} + \mu_A \quad (\text{A17})$$

$$\Delta H_B^{\alpha_k} = \varepsilon_B^{\alpha_k} + \mu_A - \mu_B \quad (\text{A18})$$

and similarly for  $\Delta H_v^{\beta_l}$  and  $\Delta H_A^{\beta_l}$ .

Within this statistical mechanics model for a binary intermetallic compound, the contributions from  $PV$  and entropy are much smaller than the contributions from the internal energy, and, therefore,  $P v_0$ ,  $v_i^v$ ,  $s_0$  and  $s_i^v$  are typically considered negligible for room temperature and pressure.

## Abbreviations

$c_i^v$	Concentration of defect $i$ on the sublattice $v$
$c_v^{\text{Ni}}$	Concentration of vacancies on the Ni sublattices
$c_v^{\text{Zr}}$	Concentration of vacancies on the Zr sublattices
$c_{\text{Zr}}^{\text{Ni}}$	Concentration of Zr anti-site atoms in the Ni sublattices
$c_{\text{Ni}}^{\text{Zr}}$	Concentration of Ni anti-site atoms in the Zr sublattices
DFT	Density functional theory
EDS	Energy dispersive spectroscopy
$J'$	Generalized grand canonical potential
$k_B$	Boltzmann constant
$M$	Number of lattice sites
$N_A$	Number of A atoms
$N_B$	Number of B atoms
$N_i^v$	Number of defect $i$ on the sublattice $v$
MH	Metal hydride
Ni/MH	Nickel/metal hydride
$P$	Pressure
$s_0$	Entropy per atom for non-defected structure
$s_i^v$	Defect entropy formation parameter for defect $i$ on sublattice $v$
SEM	Scanning electron microscopy
$T$	Temperature
$U$	Internal energy
$v_0$	Unit-cell volume per atom for non-defected structure
$v_i^v$	Defect volume formation parameter for defect $i$ on sublattice $v$
XRD	X-ray diffraction
$Z$	Number of formula units
$\alpha_k$	$k$ th sublattice for A-site atoms
$\beta_l$	$l$ th sublattice for B-site atoms
$\Delta H_f$	Energy of formation
$\Delta H_v^{\text{Ni}}$	Effective defect formation energy for vacancies in the Ni sublattices
$\Delta H_v^{\text{Zr}}$	Effective defect formation energy for vacancies in the Zr sublattices
$\Delta H_{\text{Zr}}^{\text{Ni}}$	Effective defect formation energy for Zr anti-site atoms in the Ni sublattices
$\Delta H_{\text{Ni}}^{\text{Zr}}$	Effective defect formation energy for Ni anti-site atoms in the Zr sublattices
$\varepsilon_0$	Energy per atom for non-defected structure
$\varepsilon_i^v$	Defect energy formation parameter for defect $i$ on sublattice $v$
$\mu_A$	Chemical potential for A atom
$\mu_B$	Chemical potential for B atom

## References

- Joubert, J.M.; Latroche, M.; Percheron-Guégan, A.; Bouet, J. Improvement of the electrochemical activity of Zr–Ni–Cr laves phase hydride electrodes by secondary phase precipitation. *J. Alloy. Compd.* **1996**, *240*, 219–228. [[CrossRef](#)]
- Young, K.; Nei, J.; Ouchi, T.; Fetcenko, M. Phase abundances in AB<sub>2</sub> metal hydride alloys and their correlations to various properties. *J. Alloy. Compd.* **2011**, *509*, 2277–2284. [[CrossRef](#)]
- Young, K.; Ouchi, T.; Fetcenko, M.A.; Mays, W.; Reichman, B. Structural and electrochemical properties of Ti<sub>1.5</sub>Zr<sub>5.5</sub>V<sub>x</sub>Ni<sub>10–x</sub>. *Int. J. Hydrog. Energy* **2009**, *34*, 8695–8706. [[CrossRef](#)]
- Joubert, J.M.; Latroche, M.; Percheron-Guégan, A. Hydrogen absorption properties of several intermetallic compounds of the Zr Ni system. *J. Alloy. Compd.* **1995**, *231*, 494–497. [[CrossRef](#)]
- Young, K.; Ouchi, T.; Liu, Y.; Reichman, B.; Mays, W.; Fetcenko, M. Structural and electrochemical properties of Ti<sub>x</sub>Zr<sub>7–x</sub>Ni<sub>10</sub>. *J. Alloy. Compd.* **2009**, *480*, 521–528. [[CrossRef](#)]
- Young, M.; Chang, S.; Young, K.; Nei, J. Hydrogen storage properties of ZrV<sub>x</sub>Ni<sub>3.5–x</sub> ( $x = 0.0–0.9$ ) metal hydride alloys. *J. Alloy. Compd.* **2013**, *580*, S171–S174. [[CrossRef](#)]
- Myers, S.M.; Baskes, M.I.; Birnbaum, H.K.; Corbett, J.W.; DeLeo, G.G.; Estreicher, S.K.; Haller, E.E.; Jena, P.; Johnson, N.M.; Kirchheim, R.; et al. Hydrogen interactions with defects in crystalline solids. *Rev. Mod. Phys.* **1992**, *64*, 559–617. [[CrossRef](#)]
- Chen, K.C.; Peterson, E.J.; Thoma, D.J. HfCo<sub>2</sub> laves phase intermetallics—Part I: Solubility limits and defect mechanisms. *Intermetallics* **2001**, *9*, 771–783. [[CrossRef](#)]

9. Chen, K.C.; Chu, F.; Kotula, P.G.; Thoma, D. HfCo<sub>2</sub> laves phase intermetallics—Part II: Elastic and mechanical properties as a function of composition. *Intermetallics* **2001**, *9*, 785–798. [[CrossRef](#)]
10. Ovshinsky, S.R.; Fetcenko, M.A.; Ross, J. A nickel metal hydride battery for electric vehicles. *Science* **1993**, *260*, 176–181. [[CrossRef](#)] [[PubMed](#)]
11. Züttel, A. Materials for hydrogen storage. *Mater. Today* **2003**, *6*, 24–33. [[CrossRef](#)]
12. Young, K. Stoichiometry in inter-Metallic Compounds for Hydrogen Storage Applications. In *Stoichiometry and Materials Science—When Numbers Matter*; Innocenti, A., Kamarulzaman, N., Eds.; InTech: Rijeka, Croatia, 2012; pp. 147–172.
13. Stein, F.; Palm, M.; Sauthoff, G. Structure and stability of Laves phases. Part I. Critical assessment of factors controlling Laves phase stability. *Intermetallics* **2004**, *12*, 713–720. [[CrossRef](#)]
14. Moura, C.S.; Motta, A.T.; Lam, N.Q.; Amaral, L. Atomistic simulations of point defects in zrni intermetallic compounds. *Nucl. Instrum. Methods Phys. Res. Sect. B Beam Interact. Mater. At.* **2001**, *180*, 257–264. [[CrossRef](#)]
15. Mayer, J.; Elsasser, C.; Fahnle, M. Concentrations of atomic defects in B2-Fe<sub>x</sub>Al<sub>1-x</sub>—An ab-initio study. *Phys. Status Solidi B Basic Res.* **1995**, *191*, 283–298. [[CrossRef](#)]
16. Mayer, J.; Fahnle, M. On the meaning of effective formation energies, entropies and volumes for atomic defects in ordered compounds. *Acta Mater.* **1997**, *45*, 2207–2211. [[CrossRef](#)]
17. Meyer, B.; Fahnle, M. Atomic defects in the ordered compound B2-NiAl: A combination of ab initio electron theory and statistical mechanics. *Phys. Rev. B* **1999**, *59*, 6072–6082. [[CrossRef](#)]
18. Rasamny, M.; Weinert, M.; Fernando, G.; Watson, R. Electronic structure and thermodynamics of defects in NiAl<sub>3</sub>. *Phys. Rev. B* **2001**, *64*. [[CrossRef](#)]
19. Notten, P.; Latroche, M.; Percheron-Guégan, A. The influence of Mn on the crystallography and electrochemistry of nonstoichiometric AB<sub>5</sub>-type hydride-forming compounds. *J. Electrochem. Soc.* **1999**, *146*, 3181–3189. [[CrossRef](#)]
20. Okamoto, H. Ni-Zr (nickel-zirconium). *J. Phase Equilibria Diffus.* **2007**, *28*, 409–409. [[CrossRef](#)]
21. Giannozzi, P.; Baroni, S.; Bonini, N.; Calandra, M.; Car, R.; Cavazzoni, C.; Ceresoli, D.; Chiarotti, G.L.; Cococcioni, M.; Dabo, I. Quantum Espresso: A modular and open-source software project for quantum simulations of materials. *J. Phys. Condens. Matter* **2009**, *21*, 395–502. [[CrossRef](#)] [[PubMed](#)]
22. Garrity, K.F.; Bennett, J.W.; Rabe, K.M.; Vanderbilt, D. Pseudopotentials for high-throughput DFT calculations. *Comput. Mater. Sci.* **2014**, *81*, 446–452. [[CrossRef](#)]
23. Perdew, J.P.; Burke, K.; Ernzerhof, M. Generalized gradient approximation made simple. *Phys. Rev. Lett.* **1996**, *77*, 3865–3868. [[CrossRef](#)] [[PubMed](#)]
24. Methfessel, M.; Paxton, A.T. High-precision sampling for brillouin-zone integration in metals. *Phys. Rev. B* **1989**, *40*, 3616–3621. [[CrossRef](#)]
25. Monkhorst, H.J.; Pack, J.D. Special points for brillouin-zone integrations. *Phys. Rev. B* **1976**, *13*, 5188–5192. [[CrossRef](#)]
26. Takeshita, H.T.; Fujiwara, N.; Oishi, T.; Noréus, D.; Takeichi, N.; Kuriyama, N. Another unusual phenomenon for Zr<sub>7</sub>Ni<sub>10</sub>: Structural change in hydrogen solid solution and its conditions. *J. Alloy. Compd.* **2003**, *360*, 250–255. [[CrossRef](#)]
27. Takeshita, H.; Kondo, S.; Miyamura, H.; Takeichi, N.; Kuriyama, N.; Oishi, T. Re-examination of Zr<sub>7</sub>Ni<sub>10</sub> single-phase region. *J. Alloy. Compd.* **2004**, *376*, 268–274. [[CrossRef](#)]
28. Kirkpatrick, M.; Smith, J.; Larsen, W. Structures of the intermediate phases Ni<sub>10</sub>Zr<sub>7</sub> and Ni<sub>10</sub>Hf<sub>7</sub>. *Acta Crystallogr.* **1962**, *15*, 894–903. [[CrossRef](#)]
29. Glimois, J.L.; Forey, P.; Feron, J.; Beclé, C. Structural investigations of the pseudo-binary compounds Ni<sub>10-x</sub>Cu<sub>x</sub>Zr<sub>7</sub>. *J. Less Common Met.* **1981**, *78*, 45–50. [[CrossRef](#)]
30. Joubert, J.M.; Cerný, R.; Yvon, K.; Latroche, M.; Percheron-Guégan, A. Zirconium–nickel, Zr<sub>7</sub>Ni<sub>10</sub>: Space group revision for the stoichiometric phase. *Acta Crystallogr. Sect. C Cryst. Struct. Commun.* **1997**, *53*, 1536–1538. [[CrossRef](#)]
31. Momma, K.; Izumi, F. VESTA 3 for three-dimensional visualization of crystal, volumetric and morphology data. *J. Appl. Crystallogr.* **2011**, *44*, 1272–1276. [[CrossRef](#)]
32. Eshelman, F.R.; Smith, J.F. The structure of Zr<sub>2</sub>Ni<sub>7</sub>. *Acta Crystallogr. Sect. B Struct. Crystallogr. Cryst. Chem.* **1972**, *28*, 1594–1600. [[CrossRef](#)]
33. Villars, P. Ni<sub>5</sub>Zr (ZrNi<sub>5</sub>) Crystal Structure. In *Material Phases Data System (MPDS)*; Springer-Verlag GmbH: Heidelberg, Germany, 2014.

34. Joubert, J.M.; Černý, R.; Yvon, K.; Latroche, M.; Percheron-Guégan, A. Refinement of the crystal structure of zirconium nickel,  $Zr_8Ni_{21}$ . *Z. Kristallogr. New Cryst. Struct.* **1998**, *213*, 227–228. [[CrossRef](#)]
35. Villars, P. NiZr (ZrNi) Crystal Structure. In *Material Phases Data System (MPDS)*; Springer-Verlag GmbH: Heidelberg, Germany, 2014.
36. Nash, P.; Jayanth, C.S. The Ni-Zr (nickel-zirconium) system. *Bull. Alloy Phase Diagr.* **1984**, *5*, 144–148. [[CrossRef](#)]
37. Young, K. Metal Hydrides. In *Elsevier Reference Module in Chemistry, Molecular Sciences and Chemical Engineering*; Elsevier B.V.: Waltham, MA, USA, 2013.
38. Wong, D.F.; Young, K.; Ng, K.Y.S. First-principles study of structure, initial lattice expansion, and pressure-composition-temperature hysteresis for substituted  $LaNi_5$  and  $TiMn_2$  alloys. *Model. Simul. Mater. Sci. Eng.* 2016, submitted for publication.
39. Schott, V.; Fähnle, M. Concentration of atomic defects in ordered compounds: Canonical and grandcanonical formalism. *Phys. Status Solidi B* **1997**, *204*, 617–624. [[CrossRef](#)]



© 2016 by the authors; licensee MDPI, Basel, Switzerland. This article is an open access article distributed under the terms and conditions of the Creative Commons Attribution (CC-BY) license (<http://creativecommons.org/licenses/by/4.0/>).